Title

Quantitative optical coherence elastography of the optic nerve head in vivo

Journal

IEEE Transactions on Biomedical Engineering, PP(99)

ISSN

0018-9294

Authors

Zhang, Fengyi

Li, Runze

Li, Yan

et al.

Publication Date

2023-09-18

DOI

10.1109/tbme.2023.3316606

Quantitative optical coherence elastography of the optic nerve head in vivo

Fengyi Zhang[1]‡, Runze Li[2]‡, Yan Li[1], Zhikai Zhu[1], Qifa Zhou[2]* and *Zhongping Chen*[1]*

***Abstract*— *Objective:* Optical coherence elastography (OCE) was used to demonstrate the relationship between the elasticity of the optic nerve head (ONH) and different intraocular pressure (IOP) levels in an in-vivo rabbit model for the first time. *Method:* Both ex-vivo and in-vivo rabbit ONH were imaged using OCE system. A mechanical shaker initiated the propagation of elastic waves, and the elasticity of the ONH was determined by tracking the wave propagation speed. The elasticity of the ONH under varying IOP levels was reconstructed based on the wave speed. Notably, the ONH exhibited increased stiffness with elevated IOP. *Results:* In the in-vivo rabbit models, the Young's modulus of ONH increased from 14 kPa to 81 kPa with the IOP increased from 15 mmHg to 35 mmHg. This revealed a positive correlation between the Young's modulus of the ONH and intraocular pressure. *Conclusion:* The OCE system proved effective in measuring the mechanical properties of ONH at different IOP levels, with validation in an in-vivo rabbit model. *Significance:* Considering ONH plays a critical role in vision and eye diseases, the capability to image and quantify in vivo ONH biomechanical properties has great potential to advance vision science research and improve the clinical management of glaucoma patients.**

***Index Terms*— Biomedical imaging; optical coherence elastography; optic nerve head; glaucoma.**

I. Introduction

Glaucoma is the second leading cause of blindness worldwide. At least 60 million people have been affected and the number of patients is increasing [1]. It is a chronic progressive optic neuropathy that damages the visual function systematically in different levels, such as photoreceptors and retinal ganglion cells (RGC) [2]. Although the mechanism of glaucoma is not clear, it is most likely that the central pathophysiology is caused by the damage of RGC axons of the optic nerve head (ONH) [3]. The ONH has attracted much attention for its unique discontinuity in the cornea-scleral shell which bears the dynamic load or force in the mechanical systems [4,5]. Elevated intraocular pressure (IOP) has been seen to be the primary risk factor for the progression of glaucoma. It generates overload in the ONH and makes the ONH to be stiff and distorted, which eventually leads to optic nerve axon degeneration and RGC death [6,7]. Therefore, an improved understanding of how the elevated IOP affects the biomechanical property of ONH is crucial.

Many research groups have investigated the mechanical compliance of the ONH and the surrounding sclera, using techniques such as tensile testing [8], optical coherence tomography (OCT) [9], and ultrasound speckle imaging [10]. However, there are limitations while applying these techniques on in-vivo ONH. Tensile tests can only be performed in vitro. Ultrasound imaging has a relatively low resolution. Traditional OCT can only provide the anatomical structure of the tissue. There is a need to develop a novel technique to provide the quantitative analysis of in-vivo biomechanical properties.

Elastography is a promising technique that holds the potential to reconstruct the biomechanics of the tissue quantitatively and non-invasively. Recently, both ultrasonic elastography and optical coherence elastography have been used to reconstruct the in vitro biomechanics of the ONH in different IOP levels [11, 12]. However, there is a lack of in vivo ONH experiments. Compared with ultrasound elastography, OCE gains the advantage of high resolution, but the imaging penetration depth is limited. Owing to the transparency of ocular tissues such as the cornea and vitreous humor, OCE avoids this limitation and gains more advantages in the field of ophthalmology to meet the need for high resolution [13]. In our previous work, we have successfully implemented this technology to investigate the biomechanics of the cornea [14, 15], lens [13], and retina [16, 17] in vivo. To generate the tissue deformation and initiate the elastic wave propagation, an external pushing force is necessary, such as air-puff[18], acoustic radiation force (ARF) [14], and mechanical shaker [19]. Air puff mainly has the limitation of high attenuation of the force, especially for deep tissue such as ONH, and ARF suffers from safety concerns of the ultrasound exposure in the field of ophthalmology [20]. A mechanical shaker has been used as the pushing source in elastography for ocular tissues, and surface waves were generated with no complexity reported [21]. However, in vivo mapping of ONH has not been reported.

In this study, we report the development of a high-resolution and high-speed shaker-based OCE system that enables in-vivo imaging and quantification of ONH biomechanical properties with different IOP levels. We demonstrate, to the best of our

This paper is submitted on 4/4/2023. This research was funded by Grant from the National Institution of Health (R01EY-028662, R01HL-127271, R01EB-030024, R01EB-030558)

Fengyi Zhang, Yan Li, Zhikai Zhu and Zhongping Chen were with University of California, Irvine, Irvine, California, United States (correspondence e-mail: z2chen@uci.edu). Runze Li and Qifa Zhou were with University of Southern California, Los Angeles, California, United States; (correspondence e-mail: qifazhou@usc.edu).

knowledge, the first in-vivo reconstruction of ONH biomechanical properties in a rabbit animal model.

II. Method

A. System settings

The schematic diagram of the experimental setup is shown in Figure 1. A custom phase-resolved SD-OCT system using a superluminescent diode (SLED) laser source (Superlum, USA) is developed to visualize the shear wave propagation on the ONH. The center wavelength of the light source is 890 nm, the bandwidth is 144 nm, and the output power is 9 mW. The laser beam from the SLED is filtered through an optical isolator, and the output beam is split into a sample arm and a reference arm by a 20:80 fiber optic coupler, respectively. The output power in the sample arm is about 2mw, which is within the ANSI safety range. After the optical collimator collimates the beam in the sample arm, 2D scanning is achieved by using a dual-axis galvanometer system, which can be used for MB-mode scanning protocol and volume scanning of 3D images. The sample beam is then focused onto the object by a scan lens. The backscattered signal from the sample arm is coupled with the reflected reference arm signal, and the interference signal is detected by a homemade spectrometer. A mechanical shaker (mini-shaker type 4810; Bruel & Kjaer, Duluth, Georgia, USA) was used to induce tissue motion and initiate elastic waves. For the in-vivo image, the rod tip of the shaker was positioned on the corneal limbus and aligned parallel to the OCT scanning beam while performing real-time phase-resolved OCT imaging. The scanning galvanometer mirror positioning system (galvo) was set with a step size of 3 µm, and a total of 1000 positions were scanned. The radius of the rod used was 0.4 mm, which also determines the contact area. The position of the optic nerve head (ONH) was confirmed by examining its morphology in real-time OCT B-mode imaging.

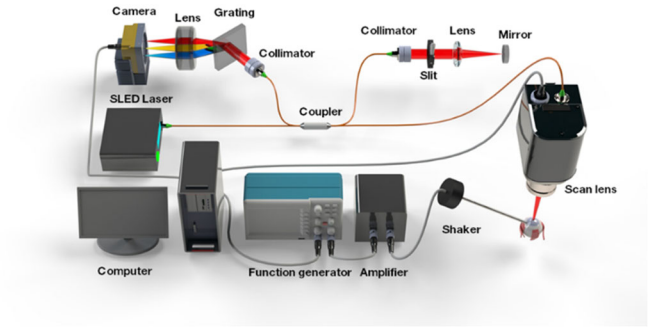

Fig. 1. Schematics of the shaker-based OCE system

The control and detection device of rabbit eye IOP is shown in Figure 2. The reservoir containing the PBS solution is attached to the eye through a 23G needle, and the IOP can be adjusted by changing the height of the reservoir. An additional small hole is made in the sclera near the fundus, and the probe of the IOP detection device is placed in the eye to detect the IOP. Before each measurement of elasticity in different IOPs, IOP is kept stable for at least three minutes to eliminate the effect of the IOP fluctuation.

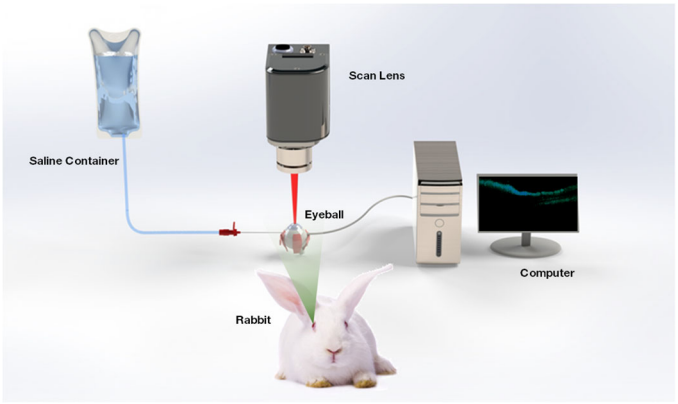

Fig. 2. IOP control and detection system

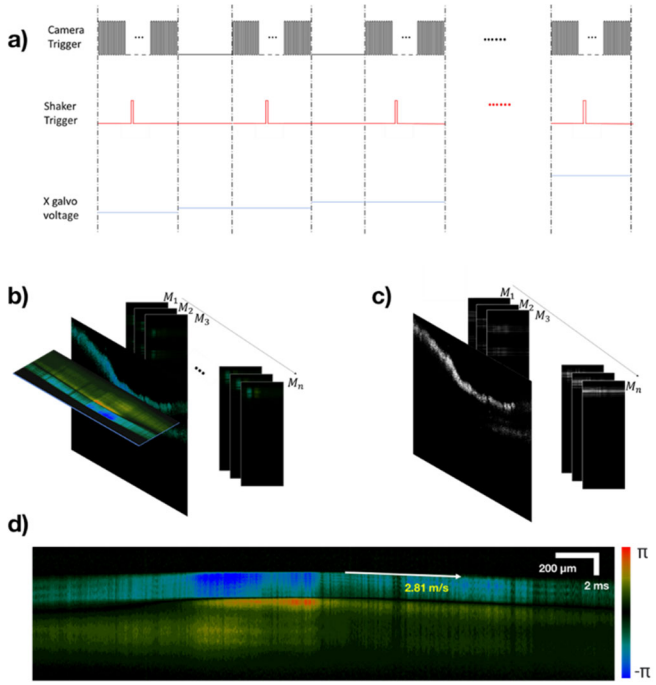

Fig. 3. Timing diagram of the MB scanning mode and the OCT images (a) Timing diagram of the MB- mode scanning protocol (b) Phase-resolved OCT sequences of MB-mode (c) OCT sequences of MB-mode (d) Spatiotemporal phase-resolved OCT image

B. System synchronization

For the visualization of the shear wave propagation in the temporal and spatial domains, a scanning protocol of MB mode is applied as follows. In an M-mode scan, 400 A-lines raw data are acquired at a single location with a sampling rate of 50 kHz, while the shaker generates the excitation at the 100th A-line scan. After one M-mode data acquisition, the galvanometer scanner moves the detection beam to the next position, and the same M-mode scan is repeated until the last imaging position. The timing diagram of the scanning protocol and the corresponding acquired OCT images are shown in Figure 3. The computer generates the trigger signals for the camera acquisition and the shaker, and are precisely synchronized to

meet the high phase stability requirements of the phase-resolved OCT imaging.

C. Mechanical characterization

The Doppler-shifted OCT signal can be detected by acquiring the full fringe signal and calculating the local frequency shift across A-lines. Moreover, the phase difference between points in successive A-lines, $\Delta\varphi$, can also be used for calculating the Doppler frequency shift, Δf, that is due to the scattering of light from moving particles and is given by [22]

$$\Delta f = \frac{\Delta\varphi}{T} \tag{1}$$

where T is the time interval between consecutive A-line scans. In the phase-resolved OCT imaging, a phase profile of OCT images can be obtained using the following equation:[23]

$$\Delta\varphi = arctan\frac{Re(I_m \times I_{m+1}^*)}{Im(I_m \times I_{m+1}^*)} \tag{2}$$

Where $Im()$ and $Re()$ are the imaginary and real parts of the OCT complex signal, respectively, I_m is the complex signal of given position on each A-line, I_{m+1} is a complex signal at the same depth of next A-line, and I_m^* is the conjugate complex of I_m. In phase-resolved OCE imaging, the displacement due to the elastic wave can be determined by the following equation:

$$\Delta d = \frac{\lambda_0 \Delta\varphi}{4\pi n} \tag{3}$$

Where λ_0 is the central wavelength, n is the refractive index. In the M-B mode OCE images, the spatiotemporal profile of displacements (Δd) can be visualized, so the elastic wave propagation on the tissue can thus be acquired. The elastic wave velocity C_s can be determined by the slope of Δd(t) in the phase-resolved spatiotemporal images.

The elastic wave propagation on the tissue can be approximated as the shear wave to quantify the elasticity of tissues, and the shear wave elastography has been widely applied in clinical use [24, 25]. Assuming the object as a homogeneous medium consisting of a single spring and damper, the shear wave velocity, C_s, is approximated using the Voigt model to quantify the body elasticity [26]. In the Voigt model for an isotropic homogeneous medium, the shear modulus can be expressed as the following equation:

$$\mu = \rho C_s^2 \tag{4}$$

Where μ is the shear modulus and ρ is the tissue density. Assuming that the tissue is incompressible and infinite, the Poisson's ratio is 0.5. Therefore, the Young's modulus can be expressed as follows:

$$E = 2(1+v)\mu = 3\rho C_s^2 \tag{5}$$

Where v is the Poisson ratio. In this research, the above model is used to estimate Young's modulus and quantify the elasticity of the tissue.

D. Ex-vivo rabbit experiment preparation

All rabbit experiments were performed in accordance with the guidelines established by the Institutional Animal Care and Use Committee (IACUC) of the University of California, Irvine. Two eyeballs of each healthy rabbit within one hour after euthanasia were harvested. 6 fresh rabbit eyeballs in total were obtained from New Zealand rabbits that were sacrificed at the end of a licensed study. A sponge holder was used to immobilize the stereoscopic eyeball. During the imaging experiment, the IOP was manipulated from normal to several higher levels to evaluate the elasticity of the ONH.

E. In-vivo rabbit experiment preparation

Six eyeballs in total were imaged during this study. Before imaging, general anesthesia was performed by subcutaneous injection of ketamine hydrochloride (35 mg/kg) and xylazine hydrochloride (5 mg/kg). After general anesthesia, two drops of proparacaine hydrochloride are applied topically to provide additional local anesthesia. Rabbits were placed on the imaging stage and equipped with a pulse oximeter (Ohmeda Biox® 3700 Pulse Oximeter, Pacific Medical, San Clemente, USA) to monitor the heart rate and oxygen saturation levels while unconscious. The elasticity of in-vivo ONH was detected using the shaker-based OCE system, and intraocular pressure was controlled and monitored using the intraocular pressure regulation and detection system. During the experiments, additional anesthesia was performed by redosing 17.5 mg/kg ketamine, which was administered every 30 min. After each experiment, rabbits were euthanized by an intravenous injection of pentobarbital.

III. Result

The New Zealand white rabbit eye is the ideal model for this study due to its similar size to the human eye. An ex-vivo rabbit ONH was imaged to test the feasibility of the proposed OCT system. Figure 4 shows one of the 2D OCT images of an ex-vivo rabbit ONH and its 3D reconstructed image. As shown in this figure, the ONH position of the rabbit eye is much deeper than the peripheral retina position. After capturing the structure of the rabbit ONH, the elasticity properties of the ONH can be obtained using phase-resolved OCT.

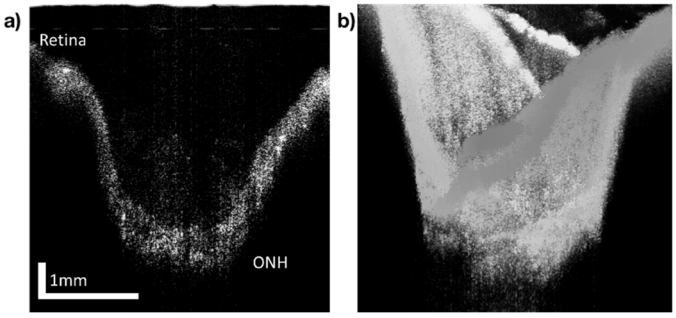

Fig. 4. a) OCT images and b) 3D reconstruction of ex-vivo rabbit ONH and peripheral retina

In this pilot study of the ex-vivo experiment, we aim the shake at the center of ONH and confirm the position from the

measurement of the elastic wave as shown in Figure 5, which demonstrated that the elastic wave was induced in the middle area. Figure 5(a) shows an OCT B-scan image of a rabbit ONH. A flat area of ONH was selected for the sake of visualizing the wave propagation. In these time-continuous OCT images, even though there are slight brightness changes in the figures, morphological changes can hardly be observed. After calculating the Doppler phase shifting, the nano-scale displacement of the tissue can be acquired, as shown in Figure 5(b). Starting at the 0.08ms of the Figure 5(b), a significant displacement can be observed at the center of the tissue, where the elastic wave was excited. As time went by, the elastic wave on the ONH propagated from the center to the edges of the ONH. According to these wave propagation image sequences, the velocity of the elastic wave can be obtained by measuring the wave propagation distances and the corresponding propagation time. Edge detection and curve compensation algorithm to reduce the calculation error induced by the curvature of the ONH. A more accurate way to determine the elastic wave velocities is to map the displacement induced by the shear wave at a certain depth over time. As shown in the Figure 5(c), the spatiotemporal phase-resolved OCT images were obtained to perform the quantification of the Young's modulus, where the vertical axis represented the temporal axis and the horizontal axis represented the spatial axis. The slope of the displacement in the ONH in the spatiotemporal phase-resolved OCT images, which is indicated by the white arrow in Figure 5(c), can be used to calculate the elastic wave velocity. The elastic wave velocities were determined by calculating the ratio of wave propagation distance to propagation time, which is 2.81 m/s in rabbit ONH. According to eq.4, the Young's modulus of ONH is determined to be 23.69kPa.

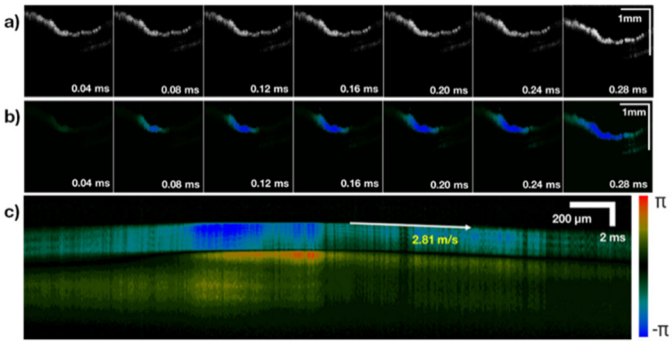

Fig. 5. Ex-vivo ONH OCT and elastography. (a) Time-lapse OCT B-scan images of an ONH. (b) Time-lapse phase-resolved OCT B-scans of an ONH. (c) Spatiotemporal phase-resolved OCT of the ONH

A. *Ex-vivo rabbit experiment*

To investigate the relationships between the IOP and the ONH edacity properties, the same measurement was performed on the ONH while elevating the IOP. As shown in Figure 6(b), the elastic wave propagation can be observed in the phase-resolved OCT images. The wave propagation speed can be calculated using the phase-resolved spatiotemporal map, as shown in Figure 6(c). With the IOP increasing, the wave propagation speed was increased, and so was the reconstructed Young's modulus. As shown in Figure 6(d), the Young's modulus of the ONH was 22.52 kPa, 28.09 kPa, and 38.99 kPa with IOP at 15, 20, and 25 mmHg, respectively.

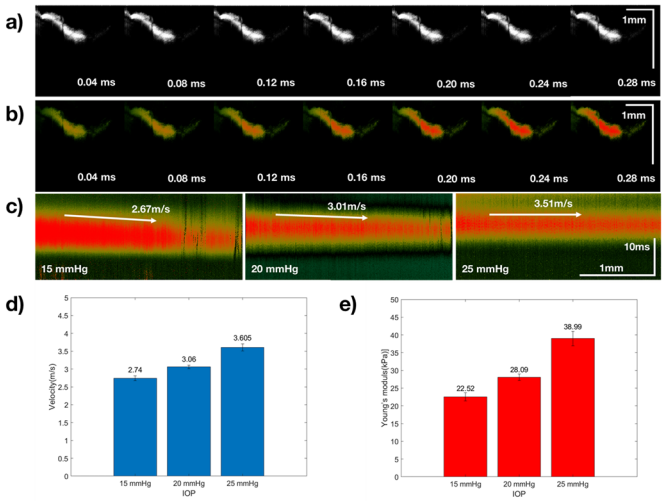

Fig. 6. Elasticity of the ex-vivo ONH. (a) Time-lapse OCT B-scan images of an ONH. (b) Time-lapse phase-resolved OCT B-scans of an ONH. (c) Spatiotemporal phase-resolved OCT of the ONH under different IOP (d) Shear wave velocities in the ONH and (e) corresponding Young's modulus at various IOP of 6 ex-vivo eyeballs

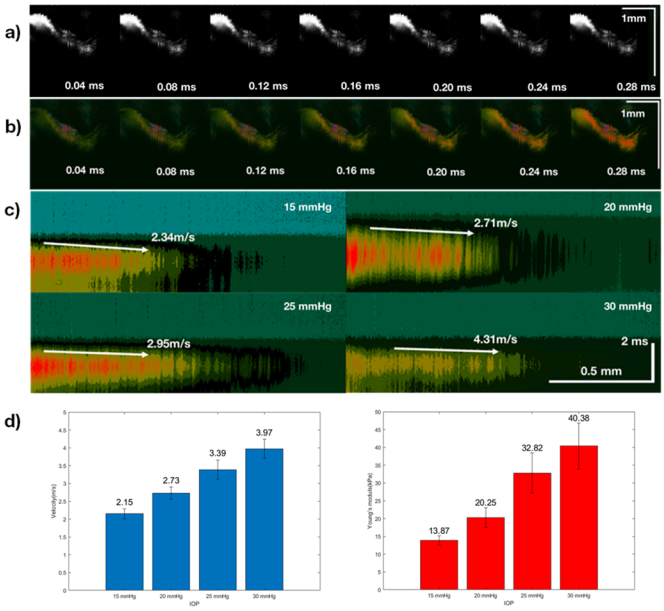

Fig. 7. Elasticity of the in-vivo ONH. (a) Time-lapse OCT B-scan images of an ONH. (b) Time-lapse phase-resolved OCT B-scans of an ONH. (c) Spatiotemporal phase-resolved OCT of the ONH under different IOP (d) Shear wave velocities in the ONH and (e) corresponding Young's modulus as a function of IOP of 6 ex-vivo eyeballs.

B. *In-vivo rabbit experiment*

To test the feasibility of the phase-resolved OCT system on detecting in-vivo state, further experiments were conducted to test the elastic changes of the ONH using the in-vivo rabbit eyes as the model under different IOP levels. For the in vivo experiments, we aimed the shake on the side of the ONH and confirmed the position through the measurement of the elastic

wave, as shown in Figure 7, where the elastic waves propagate from right to left. The force is applied by the shaker at the corneal limbus and propagates from the anterior segment to the posterior pole of the eyeball. Although the relatively long distance between the position of the force excitation and the ONH attenuates the force of the shaker, the elastic wave signal generated at the ONH by the shaker applied at the corneal limbus is still much stronger than what is typically generated by the ultrasonic transducer. In addition, our SD-OCT has excellent phase stability and can detect the nanometers displacement. By taking advantage of the strong signal produced by the shaker and the high phase stability of our phase-resolved OCT system, we can capture the elastic wave propagation at ONH with shaker force applied at the corneal limbus as confirmed by the elastic wave detected.

Figure.7(b) shows time-lapse phase-resolved OCT B-scans of rabbit ONHs, where phase shifting induced by the blood flow can be observed on the surface and the center of the ONH. The wave propagation was visualized, and the spatiotemporal phase-resolved images can be obtained, as shown in the Figure 7(c). To avoid the error induced by blood flow, the wave propagation speed was measured at the edge of the slope. The relationship between the IOP and velocity was shown in the Figure7(d), and a linear fitting was performed in the figure. As the positive relationship of elastic wave velocity and IOP was illustrated respectively, the relationship between Young's modulus and the IOP can then be acquired, as shown in the Figure 7(e), and a fit line of quadratic equations was performed. As shown in Figure 7(e), the averaged Young's modulus of the ONH was 13.87kPa, 20.25 kPa, 32.82 kPa, and 40.38 kPa with IOP at 15, 20, 25, and 30 mmHg respectively.

IV. DISCUSSION

Although the mechanisms of the glaucoma remain controversial, the elevated IOP has been identified as the primary risk factor. Many studies have suggested that the elevated IOP alters the biomechanical property of the posterior eye and damages the ONH. Thus, the biomechanical properties of the ONH can serve as a biomarker to characterize and monitor the health of the optic nerve axis and the retinal ganglion cell, making it important for clinical diagnosis [5]. Researching the relationship between ONH biomechanical properties and IOP can therefore improve the knowledge of the progression of glaucoma and provide insight on how the elevated IOP damages the ONH and other peripheral tissues. Due to the deep position and the subtle morphological structure of the ONH, many attempts have been made to quantify the biomechanical property of the ONH. Brausmann et al. investigated the biomechanical property of both ONH and peripapillary sclera (PPS) using atomic force microscopy (AFM) and revealed that the PPS was much stiffer than the ONH [27]. Qian et al. investigated the biomechanical property of ONH and PPS using ultrasonic elastography, and point-to-point stiffness mappings with different IOP levels were presented [11]. Jan et al. investigated the microstructural changes with different IOP levels of the fibers from the posterior pole using polarized light microscopy [28]. These studies facilitated the knowledge to better understand the biomechanical property of the posterior eye. However, they either lacked the in vivo experiment or had tiny sample sizes. Owing to the deep imaging penetration depth, ultrasound elastography is a promising tool for in vivo applications to investigate the biomechanics of the optic nerve. Recently, Razek et al. used an ultrasound system (Applio 500, Canon Medical Systems Corp., Tokyo, Japan) to reconstruct the biomechanics of the optic nerve sheath in humans [29]. However, the low center frequency of the ultrasound led to an unsatisfied imaging quality which diminished the accuracy of the biomechanics estimation. OCE gains the advantages in the ophthalmologic applications not only for the high resolution of this imaging modality but also the unique transparency of the lens and vitreous which provides the optical pathway to the posterior eye. These advantages enable better imaging quality and more accurate biomechanics reconstruction. In this study, we present, for the first time, a measure of the real-time elasticity of in vivo ONH at different IOPs.

A mechanical shaker-based OCE system was developed to generate the elastic wave and detect the wave velocity in the ONH, the measured wave speed was used to reconstruct the biomechanical property of the ONH. We have imaged ONH elasticity under different IOPs, both in vivo and ex vivo results indicate that the elasticity of the ONH had a positive relationship with the IOP levels. Our results showed that the Young's modulus of the ONH had a second polynomial relation with the IOP. This finding was comparable with the previous studies and implied that the high IOP levels could increase the stiffness significantly which led to damage of the posterior eye

A mechanical shaker was used to generate the elastic wave in this study. Compared with the ultrasonic transducer used in the previous study, the shaker cannot be confocal with the OCT, and the elastic wave generated is not a pure shear wave, which may induce a bias in the estimation of the elastic wave speed. However, we have confirmed in previous studies that the wave velocity had no significant difference between confocal and non-confocal alignment [19]. In addition, the use of the shaker has some advantages compared with the ultrasonic transducers, such as it is easy-to-use, and holds the potential for clinical translation.

Although we have uncovered the relationship between the IOP and ONH elasticity quantitatively using a shear wave model, some challenges remain in translating this technique for clinical use. First, the imaging speed of the system needs to be improved. Higher imaging speed can help to reduce the data acquisition time, minimize motion artifacts during in vivo experiments, and enable better detection of faster waves. One of our current OCE systems uses a swept light source, where the imaging speed is limited by the speed of the light source sweep (200 kHz). However, a variety of frequency-swept lasers that offer laser repetition rates in the megahertz range have recently been commercialized and can be used to increase imaging speeds [30]. Second, the image quality of our OCT results is not optimal compared to previous OCT images. One reason is that the unique shape and location of the rabbit eye ONH make it difficult to focus the beam without aberration. Another reason is that during the use of the IOP regulating

device, the elevated IOP causes the cornea to swell, and the endothelial cells are destroyed, resulting in blurring. In the future, we will further improve the implantation method of the IOP system to prevent eye blur. Finally, since the ONH contains various complex tissue structures, such as blood vessels and nerves, the elasticity in different positions and directions may be non-uniform. Therefore, mapping of elastic wave propagation in 3D is important for accurate measurement of ONH elasticity and for gaining insight on the effect of ONH elasticity in the progression of glaucoma.

V. CONCLUSION

In conclusion, we report the first in vivo measurement of ONH elasticity. Our OCE system is capable of measuring the mechanical properties of ONHs at different IOPs, and our technique has been validated in an in-vivo rabbit model. Since ONH plays a critical role in vision and eye diseases, the capability to image and quantify ONH biomechanical properties has great potential to advance vision science research and improve the clinical management of glaucoma patients.

REFERENCES

[1] H. A. Quigley and A. T. Broman, "The number of people with glaucoma worldwide in 2010 and 2020," British Journal of Ophthalmology, vol. 90, no. 3, p. 262, 2006, doi: 10.1136/bjo.2005.081224.

[2] R. N. Weinreb *et al.,* "The pathophysiology and treatment of glaucoma: a review," *JAMA,* vol. 311, no. 18, pp. 1901-11, May 14 2014, doi: 10.1001/jama.2014.3192.

[3] M. C. Leske *et al.*, "Factors for glaucoma progression and the effect of treatment: the early manifest glaucoma trial," *Arch Ophthalmol,* vol. 121, no. 1, pp. 48-56, Jan 2003, doi: 10.1001/archopht.121.1.48.

[4] M. Hidalgo-Aguirre *et al*., "Automatic segmentation of the optic nerve head for deformation measurements in video rate optical coherence tomography," (in eng), J Biomed Opt, vol. 20, no. 11, p. 116008, Nov 2015, doi: 10.1117/1.Jbo.20.11.116008.

[5] A. J. Bellezza *et al.,* "The optic nerve head as a biomechanical structure: Initial finite element modeling," (in English), *Invest Ophth Vis Sci,* vol. 41, no. 10, pp. 2991-3000, Sep 2000. [Online]. Available: <Go to ISI>://WOS:000089089100024.

[6] R. D. Fechtner and R. N. Weinreb, "Mechanisms of Optic-Nerve Damage in Primary Open-Angle Glaucoma," (in English), *Surv Ophthalmol,* vol. 39, no. 1, pp. 23-42, Jul-Aug 1994, doi: Doi 10.1016/S0039-6257(05)80042-6.

[7] C. F. Burgoyne *et al.,* "The optic nerve head as a biomechanical structure: a new paradigm for understanding the role of IOP-related stress and strain in the pathophysiology of glaucomatous optic nerve head damage," (in English), *Prog Retin Eye Res,* vol. 24, no. 1, pp. 39-73, Jan 2005, doi: 10.1016/j.preteyeres.2004.06.001.

[8] E. Spoerl *et al*., "The influence of various substances on the biomechanical behavior of lamina cribrosa and peripapillary sclera," (in English), *Invest Ophth Vis Sci,* vol. 46, no. 4, pp. 1286-1290, Apr 2005, doi: 10.1167/iovs.04-0978.

[9] M. A. Fazio *et al*., "In vivo optic nerve head mechanical response to intraocular and cerebrospinal fluid pressure: imaging protocol and quantification method," (in eng), Sci Rep, vol. 8, no. 1, p. 12639, Aug 23 2018, doi: 10.1038/s41598-018-31052-x.

[10] Y. H. Ma *et al.*, "Mechanical Deformation of Human Optic Nerve Head and Peripapillary Tissue in Response to Acute IOP Elevation," (in English), *Invest Ophth Vis Sci,* vol. 60, no. 4, pp. 913-920, Mar 2019, doi: 10.1167/iovs.18-26071.

[11] X. Qian *et al*., "Ultrasonic elastography to assess biomechanical properties of the optic nerve head and peripapillary sclera of the eye," (in eng), Ultrasonics, vol. 110, p. 106263, Feb 2021, doi: 10.1016/j.ultras.2020.106263.

[12] Z. Du *et al*., "Quantitative confocal optical coherence elastography for evaluating biomechanics of optic nerve head using Lamb wave model," (in eng), Neurophotonics, vol. 6, no. 4, p. 041112, Oct 2019, doi: 10.1117/1.NPh.6.4.041112.

[13] Y. Li *et al*., "Simultaneously imaging and quantifying in vivo mechanical properties of crystalline lens and cornea using optical coherence elastography with acoustic radiation force excitation," (in eng), APL Photonics, vol. 4, no. 10, Oct 2019, doi: 10.1063/1.5118258.

[14] Y. Qu *et al.*, "Acoustic Radiation Force Optical Coherence Elastography of Corneal Tissue," *IEEE J Sel Top Quantum Electron,* vol. 22, no. 3, May-Jun 2016, doi: 10.1109/JSTQE.2016.2524618.

[15] Z. Jin *et al.*, "In-vivo 3D corneal elasticity using air-coupled ultrasound optical coherence elastography," (in English), *Biomed Opt Express,* vol. 10, no. 12, pp. 6272-6285, Dec 1 2019, doi: 10.1364/Boe.10.006272.

[16] Y. Q. Qu *et al.*, "In Vivo Elasticity Mapping of Posterior Ocular Layers Using Acoustic Radiation Force Optical Coherence Elastography," (in English), *Invest Ophth Vis Sci,* vol. 59, no. 1, pp. 455-461, Jan 2018, doi: 10.1167/iovs.17-22971.

[17] R. Z. Li *et al.*, "High resolution optical coherence elastography of retina under prosthetic electrode," (in English), *Quant Imag Med Surg,* vol. 11, no. 3, pp. 918-927, Mar 2021, doi: 10.21037/qims-20-1137.

[18] S. Wang and K. V. Larin, "Noncontact depth-resolved micro-scale optical coherence elastography of the cornea," (in English), *Biomed Opt Express,* vol. 5, no. 11, pp. 3807-3821, Nov 1 2014, doi: 10.1364/Boe.5.003807.

[19] X. Qian et al., "In vivo evaluation of posterior eye elasticity using shaker-based optical coherence elastography," (in eng), Exp Biol Med (Maywood), vol. 245, no. 4, pp. 282-288, Feb 2020, doi: 10.1177/1535370219897617.

[20] X. J. Qian *et al*., "Multi-functional Ultrasonic Micro-elastography Imaging System," Scientific Reports, vol. 7, no. 1, p. 1230, 2017/04/27 2017, doi: 10.1038/s41598-017-01210-8.

[21] B. R. Zhou *et al*., "An Ultrasound Vibro-Elastography Technique for Assessing Papilledema," (in English), *Ultrasound Med Biol,* vol. 45, no. 8, pp. 2034-2039, Aug 2019, doi: 10.1016/j.ultrasmedbio.2019.04.029.

[22] Y. Zhao *et al*., "Phase-resolved optical coherence tomography and optical Doppler tomography for imaging blood flow in human skin with fast scanning speed and high velocity sensitivity," Opt. Lett., vol. 25, no. 2, pp. 114-116, 2000/01/15 2000, doi: 10.1364/OL.25.000114.

[23] Y. Zhao *et al*., "Real-time phase-resolved functional optical coherence tomography by use of optical Hilbert transformation," Opt. Lett., vol. 27, no. 2, pp. 98-100, 2002/01/15 2002, doi: 10.1364/OL.27.000098.

[24] W. T. H. Lim *et al*., "Shear Wave Elastography: A Review on the Confounding Factors and Their Potential Mitigation in Detecting Chronic Kidney Disease," (in eng), Ultrasound Med Biol, vol. 47, no. 8, pp. 2033-2047, Aug 2021, doi: 10.1016/j.ultrasmedbio.2021.03.030.

[25] M. S. Taljanovic *et al*., "Shear-Wave Elastography: Basic Physics and Musculoskeletal Applications," (in eng), Radiographics, vol. 37, no. 3, pp. 855-870, May-Jun 2017, doi: 10.1148/rg.2017160116.

[26] N. Amir *et al*., "From supersonic shear wave imaging to full-field optical coherence shear wave elastography," Journal of Biomedical Optics, vol. 18, no. 12, p. 121514, 12/1 2013, doi: 10.1117/1.JBO.18.12.121514.

[27] C. Braunsmann *et al*., "Evaluation of Lamina Cribrosa and Peripapillary Sclera Stiffness in Pseudoexfoliation and Normal Eyes by Atomic Force Microscopy," (in English), *Invest Ophth Vis Sci,* vol. 53, no. 6, pp. 2960-2967, May 2012, doi: 10.1167/iovs.11-8409.

[28] N. J. Jan and I. A. Sigal, "Collagen fiber recruitment: A microstructural basis for the nonlinear response of the posterior pole of the eye to increases in intraocular pressure," *Acta Biomater,* vol. 72, pp. 295-305, May 2018, doi: 10.1016/j.actbio.2018.03.026.

[29] A. A. K. A. Razek *et al.*, "Combined accuracy of optic nerve sheath diameter, strain ratio, and shear wave elastography of the optic nerve in patients with idiopathic intracranial hypertension," (in English), *Ultrasonography,* vol. 41, no. 1, pp. 106-113, Jan 2022, doi: 10.14366/usg.20165.

[30] J. P. Kolb *et al*., "Live video rate volumetric OCT imaging of the retina with multi-MHz A-scan rates," PLOS ONE, vol. 14, no. 3, p. e0213144, 2019, doi: 10.1371/journal.pone.0213144.